Available online at www.sciencedirect.com
SCIENCE DIRECT®

Remote Sensing of Environment 100 (2006) 223 – 236

Remote Sensing of Environment

www.elsevier.com/locate/rse

An empirical investigation of cross-sensor relationships of NDVI and red/near-infrared reflectance using EO-1 Hyperion data

Tomoaki Miura [a,*], Alfredo Huete [a], Hiroki Yoshioka [b]

[a] Department of Soil, Water and Environmental Science, University of Arizona, Tucson, AZ 85721, USA
[b] Department of Information Science and Technology, Aichi Prefectural University, Nagakute, Aichi 480-1198, Japan

Received 21 February 2005; received in revised form 19 October 2005; accepted 20 October 2005

Abstract

Long term observations of global vegetation from multiple satellites require much effort to ensure continuity and compatibility due to differences in sensor characteristics and product generation algorithms. In this study, we focused on the bandpass filter differences and empirically investigated cross-sensor relationships of the normalized difference vegetation index (NDVI) and reflectance. The specific objectives were: 1) to understand the systematic trends in cross-sensor relationships of the NDVI and reflectance as a function of spectral bandpasses, 2) to examine/identify the relative importance of the spectral features (i.e., the green peak, red edge, and leaf liquid water absorption regions) in and the mechanism(s) of causing the observed systematic trends, and 3) to evaluate the performance of several empirical cross-calibration methods in modeling the observed systematic trends. A Level 1A Hyperion hyperspectral image acquired over a tropical forest—savanna transitional region in Brazil was processed to simulate atmospherically corrected reflectances and NDVI for various bandpasses, including Terra Moderate Resolution Imaging Spectroradiometer (MODIS), NOAA-14 Advanced Very High Resolution Radiometer (AVHRR), and Landsat-7 Enhanced Thematic Mapper Plus (ETM+). Data were extracted from various land cover types typically found in tropical forest and savanna biomes and used for analyses. Both NDVI and reflectance relationships among the sensors were neither linear nor unique and were found to exhibit complex patterns and bandpass dependencies. The reflectance relationships showed strong land cover dependencies. The NDVI relationships, in contrast, did not show land cover dependencies, but resulted in nonlinear forms. From sensitivity analyses, the green peak (~550 nm) and red-NIR transitional (680 – 780 nm) features were identified as the key factors in producing the observed land cover dependencies and nonlinearity in cross-sensor relationships. In particular, differences in the extents to which the red and/or NIR bandpasses included these features significantly influenced the forms and degrees of nonlinearity in the relationships. Translation of MODIS NDVI to "AVHRR-like" NDVI using a weighted average of MODIS green and red bands performed very poorly, resulting in no reduction of overall discrepancy between MODIS and AVHRR NDVI. Cross-calibration of NDVI and reflectance using NDVI-based quadratic functions performed well, reducing their differences to ±.025 units for the NDVI and ±.01 units for the reflectances; however, many of the translation results suffered from bias errors. The present results suggest that distinct translation equations and coefficients need to be developed for every sensor pairs and that land cover-dependency need to be explicitly accounted for to reduce bias errors.

Keywords: Continuity; NDVI; Vegetation index; Reflectance; MODIS; AVHRR; ETM+; Hyperion; Cross-calibration

1. Introduction

There is a need among the science communities to advance our scientific understanding and analysis of the terrestrial carbon and biogeochemical cycles toward ultimate predictions of the Earth system behavior. This requires accurate and precise descriptions of how terrestrial vegetation functions, how it interacts with other components of the Earth system, and how it has been changing on a continuum of spatial and temporal scales.

Spectral vegetation indices (VIs) are one of the more important satellite products in monitoring temporal and spatial variations of vegetation photosynthetic activities and biophysical properties. The most widely used has been the normalized difference vegetation index (NDVI), which is the red and near-

* Corresponding author. Current address: Department of Natural Resources and Environmental Management, University of Hawai'i at Mānoa, Honolulu, HI 96822, USA.
E-mail address: tomoakim@hawaii.edu (T. Miura).

0034-4257/$ - see front matter © 2005 Elsevier Inc. All rights reserved.
doi:10.1016/j.rse.2005.10.010

infrared (NIR) reflectance difference divided by their sum (Tucker, 1979). The long term, moderate resolution dataset starting in 1980s with NOAA Advanced Very High Resolution Radiometer (AVHRR) and now transitioning to Moderate Resolution Imaging Spectroradiometer (MODIS) onboard the Terra and Aqua satellite platforms, is of great importance for monitoring ecosystem variability and response to seasonal and inter-annual environmental changes (e.g., Dong et al., 2003; Huete et al., 2002; Myneni et al., 1997; Zhang et al., 2003). Regardless of the recent failure of the Scan Line Corrector in the latest sensor, the Landsat Thematic Mapper (TM) and Enhanced Thematic Mapper Plus (ETM+) sensor series also continue to provide the high spatial resolution data base of Earth imagery begun in 1982 with the same spectral bands, enabling more detailed, consistent change detection.

These long term observations, however, require much effort to ensure continuity/compatibility due to drifts in calibration, filter degradation, and variations in band locations and/or bandwidths (e.g., Bryant et al., 2003; Che & Price, 1992; Goward et al., 1991; Kaufman & Holben, 1993). In particular, inter-sensor VI product continuity became a critical and complicated issue due to different sensor characteristics and product generation algorithms, as with AVHRR and MODIS, a requirement that needs to be addressed (Cihlar et al., 2002). There are the "horizontal" continuity issue (e.g., from AVHRR to MODIS) and the multi-scale, "vertical" continuity/compatibility issue involving simultaneous coarse to fine scale acquisitions (e.g., AVHRR and/or MODIS to ETM+ and/or Advanced Spaceborne Thermal Emission and Reflection Radiometer, ASTER). The underlying issue here is that VI values for the same targets recorded under identical conditions will not be directly comparable because input reflectance values differ from sensor to sensor (Teillet et al., 1997; Yoshioka et al., 2003).

One key sensor characteristic that varies widely among sensors is the spectral bandpass filters (BPFs) and, thus, many studies have focused on this "spectral issue." Teillet et al. (1997) showed that, for a forested region in southeastern British Columbia, the NDVI is affected by differences in bandwidth, notably of the red bands. On the other hand, the NDVI values were found to be strongly affected by the proximity of the red and NIR bands to the red edge region (690–750 nm) in a Brazilian tropical savanna region (Galvao et al., 1999). Trishchenko et al. (2002) used modeled spectral datasets to investigate the sensitivity of the NDVI and reflectance to BPFs for selected sensors, including AVHRR, MODIS, Satellite Probatoire d'Observation de la Terre (SPOT) VEGETATION, and Advanced Earth Observing Satellite II (ADEOS-II) Global Imager (GLI). Both the NDVI and reflectance were found to be sensitive to the BPFs, causing notable differences in their values not only among the sensors with large spectral characteristic differences (AVHRR, MODIS, VEGETATION, and GLI), but also among some of the AVHRR sensor series (Trishchenko et al., 2002). Recently, Gallo et al. (2004) compared the AVHRR and MODIS NDVI data over the conterminous USA and showed that the composite AVHRR NDVI data were associated with the corresponding MODIS data with over 90% of the variation explained by a simple linear relationship.

Several attempts have been made to reconcile NDVI data produced from different sensors. Trishchenko et al. (2002) developed a series of quadratic, "spectral correction" functions to translate the reflectance and NDVI of selected sensors to NOAA-9 AVHRR-equivalents, whereas Steven et al. (2003) used simple linear relationships to cross-calibrate the NDVI to a precision of 1–2% for agricultural crop monitoring. Gitelson and Kaufman (1998) attempted to generate AVHRR-equivalent NDVI data from MODIS reflectances by taking weighted averages of MODIS narrow green and red bands to simulate "AVHRR-like" MODIS NDVI. Although their analyses showed promising results, it was complicated by the fact that the optimum weights were dataset-, and thus, land cover-dependent. Another practical method for translating the NDVI from MODIS to AVHRR was proposed by Gao (2000), which re-introduced water vapor contaminations into the MODIS NIR band to simulate the broad AVHRR channel 2. Yet another approach was proposed by Yoshioka et al. (2003), which accounts for target greenness and brightness in the translations.

In the present study, we also focused on the spectral issue and investigated cross-sensor relationships of the NDVI as well as the red and NIR reflectances. The specific objectives of this study were: 1) to understand the systematic trends in cross-sensor relationships of the NDVI and reflectance as a function of spectral bandpasses, 2) to examine/identify the relative importance of the spectral features (i.e., the green peak, red edge, and leaf liquid water absorption regions) in and the mechanism(s) of causing the observed systematic trends, and 3) to evaluate the performance of several empirical cross-calibration methods in modeling the observed systematic trends. The key questions being raised here were whether or not cross-sensor relationships of the NDVI and reflectances could be generalized and, if so, could be modeled by empirical means for tropical biomes. Our approach was to spectrally aggregate hyperspectral imagery to simulate various sensor bandpasses. The image data used here were acquired over a tropical forest–savanna transitional zone in Brazil with a satellite-borne hyperspectral sensor, Hyperion, onboard the Earth Observing One (EO-1) platform (Ungar et al., 2003). The area exhibits a wide variety of land surface conditions with varying amounts of green and senescent vegetation components, which allowed for analysis of inter-sensor NDVI and reflectance relationships in their full dynamic ranges and their land cover dependencies.

2. Materials and methods

2.1. Site description

Our study area was located on a tropical forest–savanna transitional region along an eco-climatic gradient in Brazil where two distinct biomes met and co-existed (Table 1). The area consisted of a preserved national park, Araguaia National Park, surrounded by a complex mosaic of undisturbed forest/savanna and converted land areas. A wide range of land cover

Table 1
Description of the study area

Location	Santana do Araguzia, Brazil(S 9°59′/W 50°02′)
Resource area	Araguaia National Park and Surrounding Area
Biome/vegetation type	Tropical forest–savanna transition
Mean annual precipitation	1670 mm
Mean annual temperature	26 °C
Major land cover type/physiognomy	Primary forest
	Riparrian forest
	Savanna woodland
	Savanna grassland
	Cultivated pastures
	Burned savanna
	Sand beach

types typically found in Brazilian seasonal tropical forest and savanna were represented in this transitional area, including primary forest, riparian forest, savanna woodland, savanna grassland, converted pasture, and burned areas. The mean annual precipitation and temperature in this area are 1670 mm and 26 °C, respectively.

2.2. Hyperspectral image processing

A hyperspectral Hyperion image of the area was acquired in the 2001 dry season (July 18). Hyperion is a pushbroom sensor that covers a ground swath of approximately 7.5 km at 30 m spatial resolution (Pearlman et al., 2003; Ungar et al., 2003). The sensor samples the 400–2400 nm wavelength region at every 10 nm with 220 bands of 10 nm resolution. Along-track imaging lengths are controllable and this particular scene had a 180 km length, the same as that for Landsat TM and ETM+. The image was preprocessed and radiometrically calibrated into a Level 1A product at the TRW Hyperion image processing facility. There remain, however, several uncorrected known artifacts in the Level 1A products. Hence, we applied the following corrections to the image: spike noise removal, bad pixels correction, radiometric calibration adjustments, and

Table 2
Description of parameters used in the Hyperion atmospheric correction

Hyperion image acquisition date	18-July-2001
Ground elevation asl*	210 m
Solar zenith/azimuth angles	44°/134°
Atmospheric model	Tropical
Column water vapor content**	4.3 cm
Ozone content**	.265 cm-atm
Aerosol model	Continental
Visibility	100 km

* ASL – Above Sea Level: Values taken from GTOPO 30 (Gesch, 1994).
** Values taken from Level-3 MODIS Atmosphere Daily Global Product (King et al., 2003).

inter-spectrometer co-alignment (Biggar et al., 2003; Green et al., 2003; Pearlman et al., 2003).

The image was then spectrally convolved to Terra MODIS, NOAA-14 AVHRR, and Landsat-7 ETM+ solar reflective bands (Fig. 1) as well as various bandpasses used in a sensitivity analysis described in the Sections 2–4. The spectral response curves were splined to Hyperion band center wavelengths for each Hyperion pixel because each pixel had a slightly different spectral calibration (the spectral smile effect) (Green et al., 2003; Pearlman et al., 2003). The maximum difference in the center wavelength across the swath was ~3.5 nm; this difference had a significant impact when the image was spectrally convolved without accounting for the smile effect (not reported here).

The convolved image was corrected for atmosphere with the "6S" radiative transfer code to retrieve the ground reflectances, from which the NDVI were computed (Vermote et al., 1997). The 6S model was constrained with site specific atmospheric parameter values retrieved from available data sources (Table 2). The atmospheric model used for the scene was chosen based on the latitude and season. Pressure was adjusted for local ground elevation retrieved from GTOPO30 (Gesch, 1994). Total ozone thicknesses and column water vapor contents were extracted from the MODIS daily atmosphere

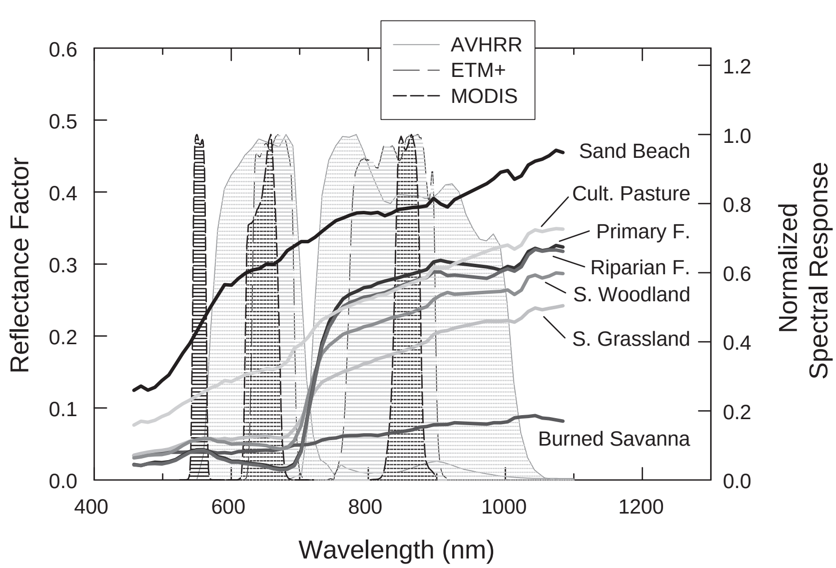

Fig. 1. Normalized bandpass filters of NOAA-14 AVHRR, Landsat-7 ETM+, and Terra MODIS in the visible-near-infrared regions superimposed onto Hyperion reflectance spectra for selected targets (S.—Savanna, F.—Forest).

product (King et al., 2003). We used the continental aerosol model with a 100 km visibility (~.1 optical thickness). Because the scene was acquired under a clear sky condition in the beginning of a dry season (before the start of a biomass burning season), this assumption was considered reasonable.

Aircraft and ground surveys were conducted within 1 week of the scene acquisition date, which found and identified seven land cover types at various locations within the scene frame. These included primary forest, riparian forest, savanna woodland, and savanna grassland as well as converted pastures as vegetated targets, and dark, burned savanna and bright, sand beach as a little or non-vegetated targets (Table 1, Fig. 1). This set of land cover types allowed for analyses to cover a wide range of target greenness and brightness with the primary forests serving as the most densely vegetated target while the burned savanna and bright sands providing a soil baseline. For each land cover type, data were extracted at 50 different locations (pixels) and used for analyses.

2.3. Analysis for existing sensor pairs

Cross-sensor relationships of the reflectances and NDVI were examined for the three sensor pairs of AVHRR vs. MODIS, ETM+ vs. MODIS, and AVHRR vs. ETM+. The first pair represented an example of the horizontal continuity, whereas the other two were used as examples of the vertical continuity. Differences in reflectances or NDVI between two sensors were computed and analyzed in order to observe trends in and land cover dependencies of the relationships in details.

2.4. Sensitivity analysis

A sensitivity analysis was conducted to empirically examine the relative importance of spectral features and mechanisms in causing the observed trends in the inter-sensor relationships. The “narrow” MODIS bands were used as a reference and their bandwidths were gradually widened toward shorter and longer wavelengths to include the three diagnostic spectral features of green vegetation covered by the AVHRR and ETM+ bandpasses: (1) the green peak (~550 nm), (2) red edge (red-NIR transitional) (680~780 nm), and (3) leaf liquid water absorption (~940 nm). To focus on the impact of these spectral features, a square response function was assumed for all these bandpass simulations.

Percent relative differences (%ΔNDVI) were used as a means of quantitatively comparing the NDVI changes or sensitivities to changes in bandwidths:

$$\%\Delta\mathrm{NDVI} = 100 \times \frac{\mathrm{NDVI}_{\pm} - \mathrm{NDVI}_{\mathrm{MODIS}}}{\mathrm{NDVI}_{\mathrm{MODIS}}}, \qquad (1)$$

where $\mathrm{NDVI}_{\pm}$ is the NDVI computed from the red and/or NIR reflectance of the wider bandwidths and $\mathrm{NDVI}_{\mathrm{MODIS}}$ is the NDVI derived from the simulated MODIS reflectances. The mean and standard deviation of the percent relative differences were derived for each land cover type and compared to assess any land cover dependencies in the NDVI sensitivities.

2.5. Evaluation of empirical methods

Several empirical cross-calibration methods attempted by the past studies can be categorized into two types: calibration by regression (Steven et al., 2003; Trishchenko et al., 2002) or by weighted averaging (Gao, 2000; Gitelson & Kaufman, 1998). Both types of empirical methods were applied to our data set to evaluate their performances in modeling the observed trends and land cover dependencies.

The spectral correction method proposed by Trishchenko et al. (2002) was used as a representative of the first category, in which the differences in reflectance or NDVI are modeled as a second order polynomial of the NDVI:

$$\Delta\rho_{\mathrm{FROM}} = \beta_0 + \beta_1\mathrm{NDVI}_{\mathrm{FROM}} + \beta_2\mathrm{NDVI}^2_{\mathrm{FROM}} + \varepsilon, \qquad (2)$$

$$\Delta\rho_{\mathrm{FROM}} = \rho_{\mathrm{FROM}} - \rho_{\mathrm{TO}}, \qquad (3)$$

and

$$\Delta\mathrm{NDVI}_{\mathrm{FROM}} = \beta_0 + \beta_1\mathrm{NDVI}_{\mathrm{FROM}} + \beta_2\mathrm{NDVI}^2_{\mathrm{FROM}} + \varepsilon, \qquad (4)$$

$$\Delta\mathrm{NDVI}_{\mathrm{FROM}} = \mathrm{NDVI}_{\mathrm{FROM}} - \mathrm{NDVI}_{\mathrm{TO}}, \qquad (5)$$

where the subscripts FROM and TO indicate the sensor to be translated (hereafter, referred to as the “source” sensor) and the “target” sensor, respectively, and ε is the unexplained error term. This approach is unique in that the NDVI is used as a predictor variable even for modeling the behaviors of reflectance differences, i.e., modeling the changes in reflectance and NDVI differences virtually as a function of greenness. Eqs. (2) and (4) were fitted to our reflectance and NDVI datasets to examine how well a quadratic function could approximate inter-sensor relationships.

For the second category, we applied the method proposed by Gitelson and Kaufman (1998):

$$\mathrm{NDVI}_{\mathrm{green+red}} = \frac{\rho_{\mathrm{NIR}} - \left[\alpha\rho_{\mathrm{green}} + (1-\alpha)\rho_{\mathrm{red}}\right]}{\rho_{\mathrm{NIR}} + \left[\alpha\rho_{\mathrm{green}} + (1-\alpha)\rho_{\mathrm{red}}\right]}. \qquad (6)$$

In this equation, the coefficient α determines the contribution of the green MODIS channel to the NDVI; $\alpha = 0$ corresponds to the ordinary NDVI derived from the red and NIR reflectances, while $\alpha = 1$ corresponds to the NDVI computed with the green band in place of the red, and $\alpha = .15$ has been suggested as the “optimized” NDVI. We computed $\mathrm{NDVI}_{\mathrm{green+red}}$ using the simulated MODIS and AVHRR spectral datasets for various α values, including $\alpha = .15$. The method of Gao (2000) was not considered because it was developed for a use in water vapor uncorrected data.

3. Results

3.1. Reflectance relationships

In Fig. 2, the differences in reflectance between the source and target sensors are plotted against the reflectances of the target sensors for three source-target pairs: AVHRR vs. MODIS

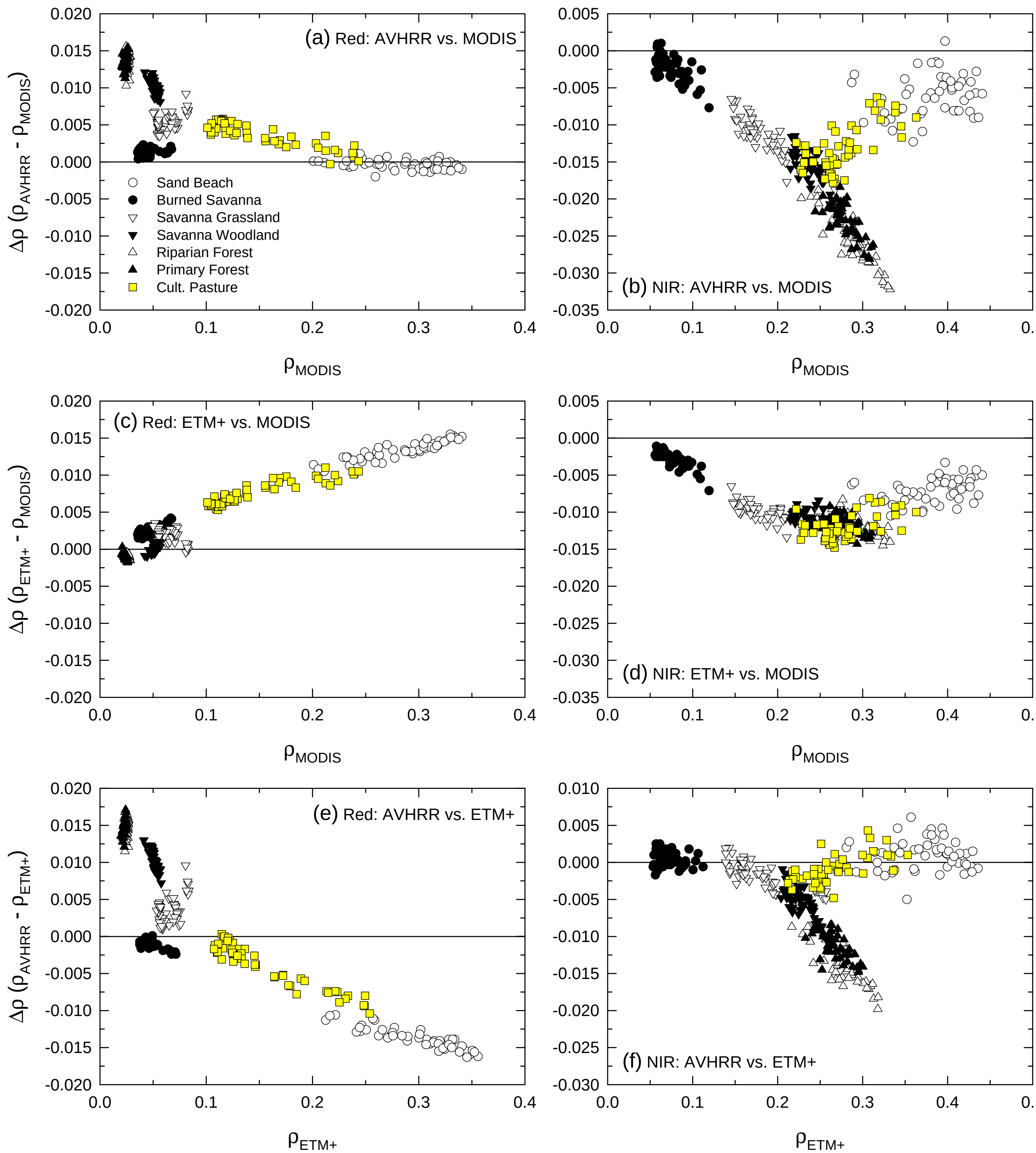

Fig. 2. Reflectance differences between source and target sensors plotted against target sensor values.

(Fig. 2a,b), ETM+ vs. MODIS (Fig. 2c,d), and AVHRR vs. ETM+ (Fig. 2e,f).

3.1.1. AVHRR vs. MODIS

The difference in red reflectance between AVHRR and MODIS varied from −.001 to .016 (Fig. 2a). The difference in the reflectance tended to decrease with increasing target brightness (reflectance value) and increased with increasing target greenness (Fig. 2a). They were small for the non-vegetated targets (i.e., burned savanna and sand beach), but large for the densely vegetated targets (i.e., riparian and primary forests). These variations, and the brightness and greenness dependencies are associated with the inclusion of the green peak (Gitelson & Kaufman, 1998) and/or red edge regions in the broader bandpass of the AVHRR channel 1 (Fig. 1).

The NIR reflectance differences were twice those of the red reflectance in terms of their magnitude range (0 to −.033) (Fig.

2b). As for the red reflectance, the NIR reflectance difference increased with increasing target greenness, with the densely vegetated targets having the largest differences. In contrast to the red reflectance, however, the NIR reflectance differences showed two distinct trends with increasing target brightness. Specifically, the difference increased nearly linearly as the target sensor reflectance value increased from .05 to .25, but as the target sensor reflectance value increased beyond .25, the differences for greener targets (savanna woodland, and riparian and primary forests) continued to increase whereas those for less green pasture and bright sand beach targets decreased with increasing reflectance. The observed trends in the NIR reflectance differences are likely due to the inclusion of either the red edge or leaf liquid water absorption regions in the broader bandpass of the AVHRR channel 2 (Fig. 1).

3.1.2. ETM+ vs. MODIS

The plot of the difference in red reflectance between ETM+ and MODIS (Fig. 2c), as well as the corresponding plot for NIR reflectance (Fig. 2d), indicate that the reflectance differences between these sensors are less land cover-dependent than those between AVHRR and MODIS. For the red reflectance, the differences were, on average, nearly zero at low reflectance values and then increased linearly with increasing reflectance (Fig. 2c). Some land cover dependencies are observed in the reflectance differences at low reflectance values (.0–.1); however, this effect may be too small to be of practical significance. We attribute these observed trends to the greater width of the ETM+ red band than the MODIS red band, with the additional width being toward longer wavelengths. The inclusion of this additional red edge region in the ETM+ band means that its reflectance values become larger than those of MODIS for targets with higher reflectance values at longer wavelengths, that is, slightly or non-vegetated areas and pastures (see Fig. 1).

The difference between the NIR reflectances of the ETM+ and MODIS sensors showed a nonlinear trend (Fig. 2d) in which the magnitude of the difference first increased (larger negative values) and then decreased (smaller negative values) with increasing reflectance value. This trend can be explained by both the greater width of the ETM+ NIR band and the relative position of the MODIS bandpass within the ETM+ bandpass. For all of the targets analyzed, the reflectance increased linearly with increasing wavelength within the ETM+ bandpass (see Fig. 1). The only difference among the land cover types was in the rate of the reflectance increase, which was low for the burned savanna and sand beach targets and high for the other targets. Because the ETM+ bandpass extends further in the short wavelength direction than in the long wavelength direction relative to the MODIS bandpass, the ETM+ reflectance values become much smaller than the MODIS values for targets whose reflectance values increase more rapidly with increasing wavelength.

3.1.3. AVHRR vs. ETM+

The general trend in the difference between the AVHRR and ETM+ red reflectance values (Fig. 2e) was similar to that observed in the difference between the AVHRR and MODIS values (Fig. 2a). The differences between the AVHRR and ETM+ red reflectance values were, however, the largest ($-.017$ to .18) and showed the largest land cover dependence among the sensor pairs examined in this study. The AVHRR red reflectance values were larger than those of ETM+ for vegetated targets, except pastures, due to the inclusion of the green peak and/or red edge regions in the AVHRR channel 1. On the other hand, the inclusion of the green peak region in the AVHRR channel 1 caused the AVHRR reflectance values for the dark, burned savanna and the bright, pastures and sand beach targets to be less than those of ETM+ because the reflectance values of these targets drop significantly in this region (see Fig. 1).

The differences in the NIR reflectances between AVHRR and ETM+ (Fig. 2f) resembled those between AVHRR and MODIS (Fig. 2b) in as much as two distinct trends were observed in the NIR reflectance relationship. In contrast to the trend for AVHRR and MODIS, however, the differences between the AVHRR and ETM+ NIR reflectances were zero on average for the non-vegetated targets regardless of the target brightness, but consistently deviated for the forest and woodland targets, forming a separate relationship. This behavior is, again, most likely due to the inclusion of the red edge region in the broader AVHRR channel 2, which lowered the reflectance values of the forest and woodland targets. The reflectance values for these targets would also be lowered by leaf liquid water absorption at ~940 nm although this effect is expected to be much smaller than that associated with including the red edge region.

3.2. NDVI relationships

The large scatterings and two distinctive trends observed in the reflectance relationships due to land cover dependencies were normalized in the inter-sensor NDVI relationships (expressed as trends in the differences), leading to the formation of single, land cover-independent relationships (Fig. 3). The difference in the AVHRR and MODIS NDVIs increased nearly linearly with increasing NDVI value from 0 at low NDVI to $-.1$ at high NDVI (Fig. 3a). In contrast, the difference between the ETM+ and MODIS NDVIs changed nonlinearly but smaller in magnitude (Fig. 3b); the differences first increased and then decreased to zero at the highest NDVI value, i.e., the two sensors gave identical values for dark, dense forest vegetation. The differences between AVHRR and ETM+ NDVIs were the largest, ranging from .02 to $-.1$, and also showed a some nonlinear trend (Fig. 3c).

The NDVI differences for the burned savanna target exhibited large secondary variations (within-land cover variations) (Fig. 3). For example, the differences between the AVHRR and MODIS NDVIs varied from $-.05$ to 0 for the burned savanna but varied only from $-.04$ to $-.02$ for the cultivated pasture at the same MODIS index value of .25 (Fig. 3a). The observation of large secondary variations was attributed to the inherent variability of the NDVI; the index is highly sensitive to small changes in the red reflectance for dark targets (e.g., Yoshioka et al., 2000).

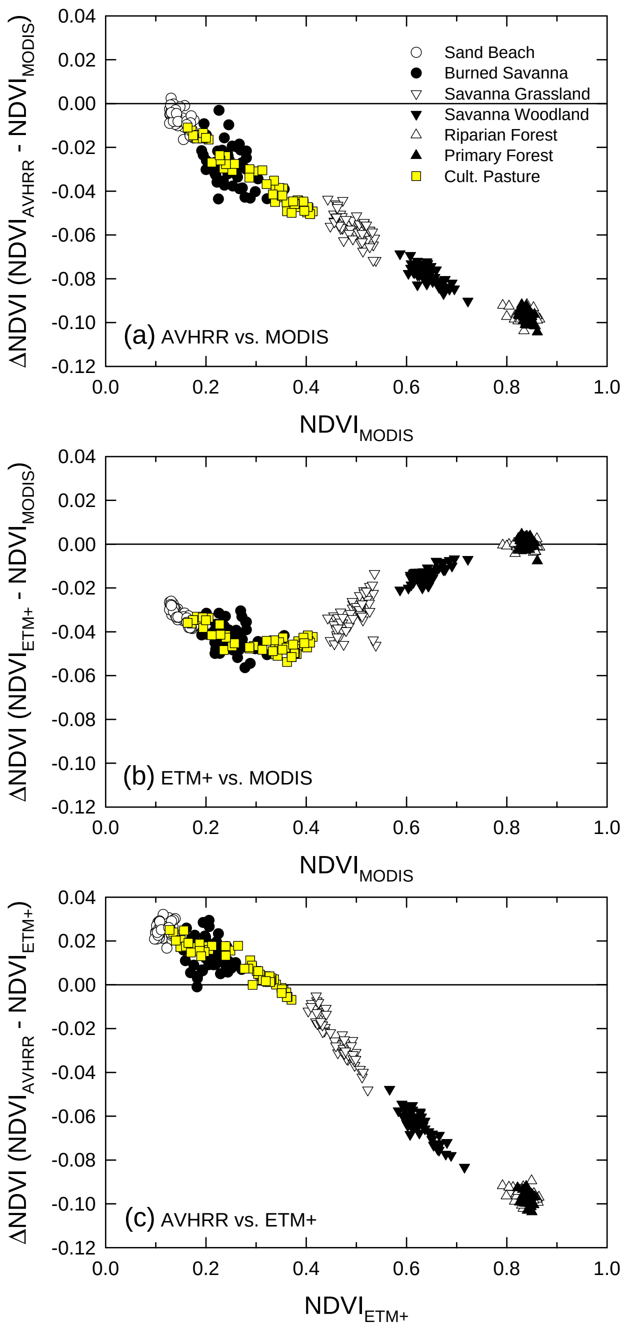

Fig. 3. NDVI differences between (a) AVHRR and MODIS, (b) ETM+ and MODIS, and (c) AVHRR and ETM+ plotted against their respective target sensor values.

3.3. Sensitivity analysis

3.3.1. Change in reflectance relationship

The simulation results for the red and NIR reflectances are shown in Fig. 4. For each of the three spectral features examined, three bandpass results are selected and plotted to clearly show the systematic changes in the trends.

The inclusion of the green peak region into the red bandpass caused an overall decrease in the reflectance (Fig. 4a). The magnitude of the decrease was larger for brighter targets, i.e., the difference values increased near-linearly (larger negative values) with increasing target brightness. Only the reflectance values for the dark, densely vegetated targets (primary forest and savanna woodland) increased in the other direction (larger positive differences) with the inclusion of the green region due to the pronounced green peak feature in their spectral reflectances (see Fig. 1). Although the increase was small (<.005), these targets deviated from the general linear trends (Fig. 4a).

Widening the red bandpass to include the red edge region consistently increased the reflectance values for all the land cover types examined (Fig. 4b). The differences increased near-linearly with increasing target brightness with those for dark, dense vegetation (forest and savanna woodland) being the smallest, when a small portion of the red edge region was included in the bandpass (≤710 nm). In addition to the target brightness, the target greenness affected the differences, but this effect was only significant when a large portion of the red edge region was included in the red bandpass (≥730 nm) (the open symbols in Fig. 4b).

The NIR reflectances were consistently smaller when the red edge region was included in the NIR bandpass (Fig. 4c). The magnitude of this decrease depended on the target greenness and brightness, leading to nonlinear trends in the reflectance differences (Fig. 4c). A separate trend for the primary forest and savanna woodland was formed only when the NIR bandpass was extended to include the sharp NIR-red transitional region (720 nm).

Inclusion of the leaf liquid water absorption region seemed to lower the reflectance values for the bright sand beach and dense green targets (primary forest and savanna woodland) (Fig. 4d). The large scatter, however, made it difficult to observe any systematic trends. Regardless, the leaf liquid water absorption appeared to have the least impact on the reflectance relationships.

The following conclusions can be drawn from the above analysis results:

1) The large, greenness-dependent scatters in the red reflectance differences at low reflectance (0–.1) observed for AVHRR vs. MODIS and AVHRR vs. ETM+ are due to both the green peak and red edge features, with the latter feature potentially having a larger impact than the former.
2) The overall linear trend in the red reflectance differences at medium to high reflectances (.1–.4) observed for AVHRR vs. ETM+ is due to the green peak feature.
3) The overall linear trend in the red reflectance differences observed for ETM+ vs. MODIS is, on the other hand, due to the red edge feature.
4) The nonlinear trend in the NIR reflectance difference observed for ETM+ vs. MODIS is due to the red edge feature.
5) The separate trends formed for the dense, green vegetation targets in the NIR reflectance differences for AVHRR vs. MODIS and AVHRR vs. ETM+ are due to the red edge feature. These separate trends appeared only because of the very broad spectral bandpass of the AVHRR channel 2.

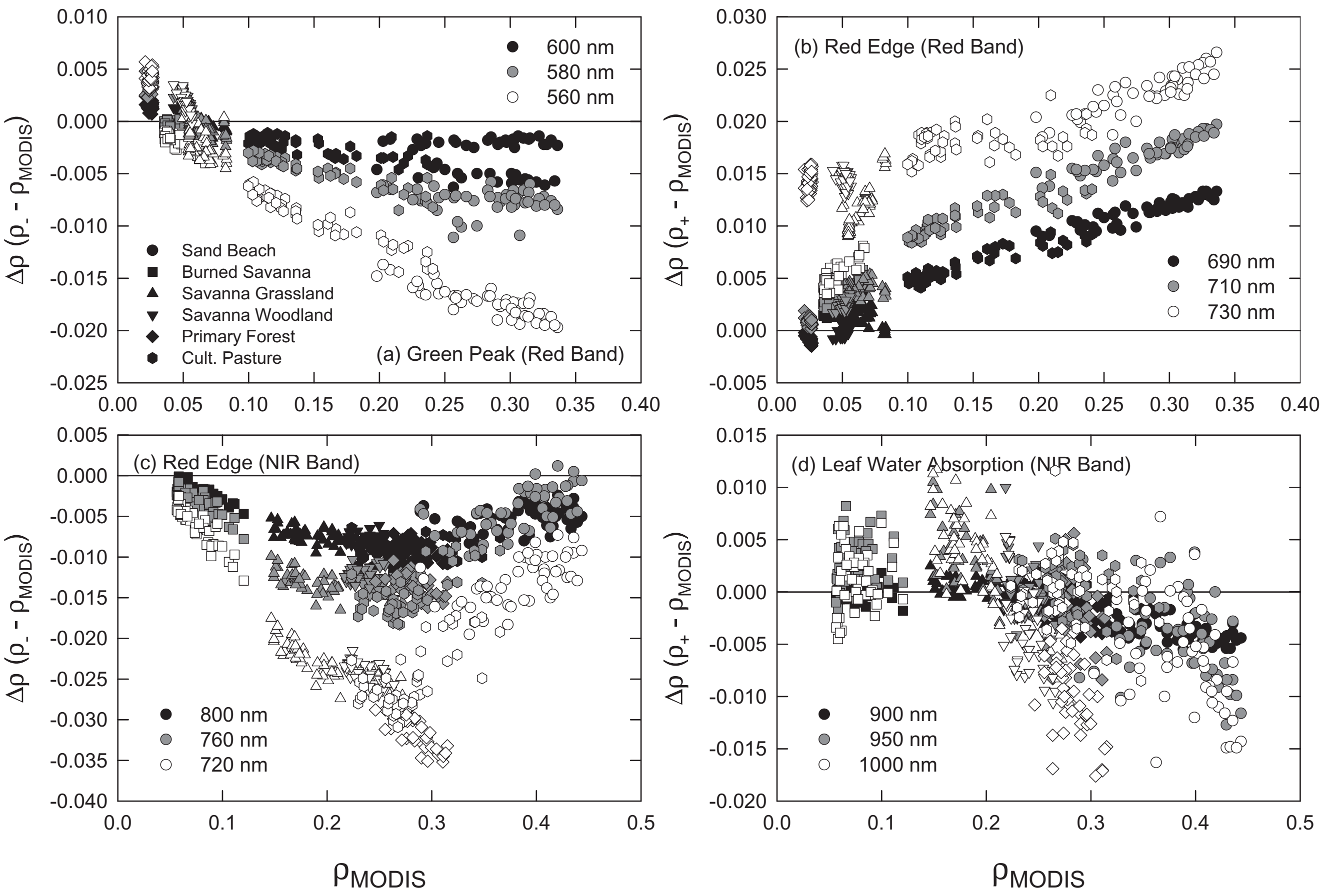

Fig. 4. Reflectance differences between widened and MODIS bandpasses plotted against MODIS reflectances for: red bandpasses widened to include (a) the green peak and (b) red edge (red-NIR transitional) features and NIR bandpasses widened to include (c) the red edge and (d) leaf liquid water absorption features. The values in the legends are the wavelengths up to which the simulated bandpasses were widened from the MODIS bandpasses. Reflectance differences for riparian forests which were nearly identical to those for primary forests are not shown for clarity.

3.3.2. Change in the NDVI relationship

The inclusion of the green peak region into the red bandpass made the NDVI relationships nonlinear (expressed as trends in the differences) (Fig. 5a). The NDVI values decreased for the dense, green vegetation targets (primary forest and savanna woodland), but increased for the other targets. The degree of nonlinearity and the differences in the NDVI values increased as the red bandpass was widened. The change in the NDVI, with increasing bandwidth for the dark, burned savanna target, was less than the overall trend (Fig. 5a).

The inter-sensor NDVI relationships also changed from linear to nonlinear when the red bandpass was widened to include the red edge region (Fig. 5b). The difference first increased (larger negative values) and then decreased (smaller negative values) with increasing NDVI. This somewhat complicated trend was maintained as the red bandpass was extended up to 710 nm, although the magnitude of the difference increased with increasing bandwidth. When the red band was widened to include a significant portion of the sharp, red-NIR transitional region, the relationships became near-linear, with the difference increasing with increasing index value (Fig. 5b).

The inclusion of the red-NIR transitional region into the NIR spectral bandpass resulted in convex shaped, nonlinear index relationships (Fig. 5c). Both the degree of nonlinearity and the magnitude of the differences increased with increasing bandwidth. Note that the separate trends for green targets observed in the reflectance relationships were normalized and not seen in the NDVI relationships (Fig. 5c).

The inclusion of the leaf liquid water absorption region caused the inter-sensor NDVI relationships to become concave although this extension of the bandpass had less effect than the others considered (Fig. 5d). The NDVI differences first increased and then decreased with increasing NDVI. Only the NDVI differences for burned savanna showed large variations, ranging from −.04 to .06; again, these variations can be associated with the relatively low signal-to-noise ratios of the Hyperion data (Fig. 5d).

The effect on the inter-sensor NDVI relationships of simultaneously widening the red and NIR bandwidths was also examined (Fig. 6). For all of the combinations, the change in the NDVI difference caused by simultaneously varying the red and NIR bandwidths was simply equal to the sum of the changes observed for the individual bands (e.g., compare Fig. 6a with the sum of Fig. 5a and c). The largest NDVI differences were observed when both the red and NIR bandwidths were widened to include the red-NIR transitional feature (Fig. 6b), which is in agreement with the findings by Galvao et al. (1999)

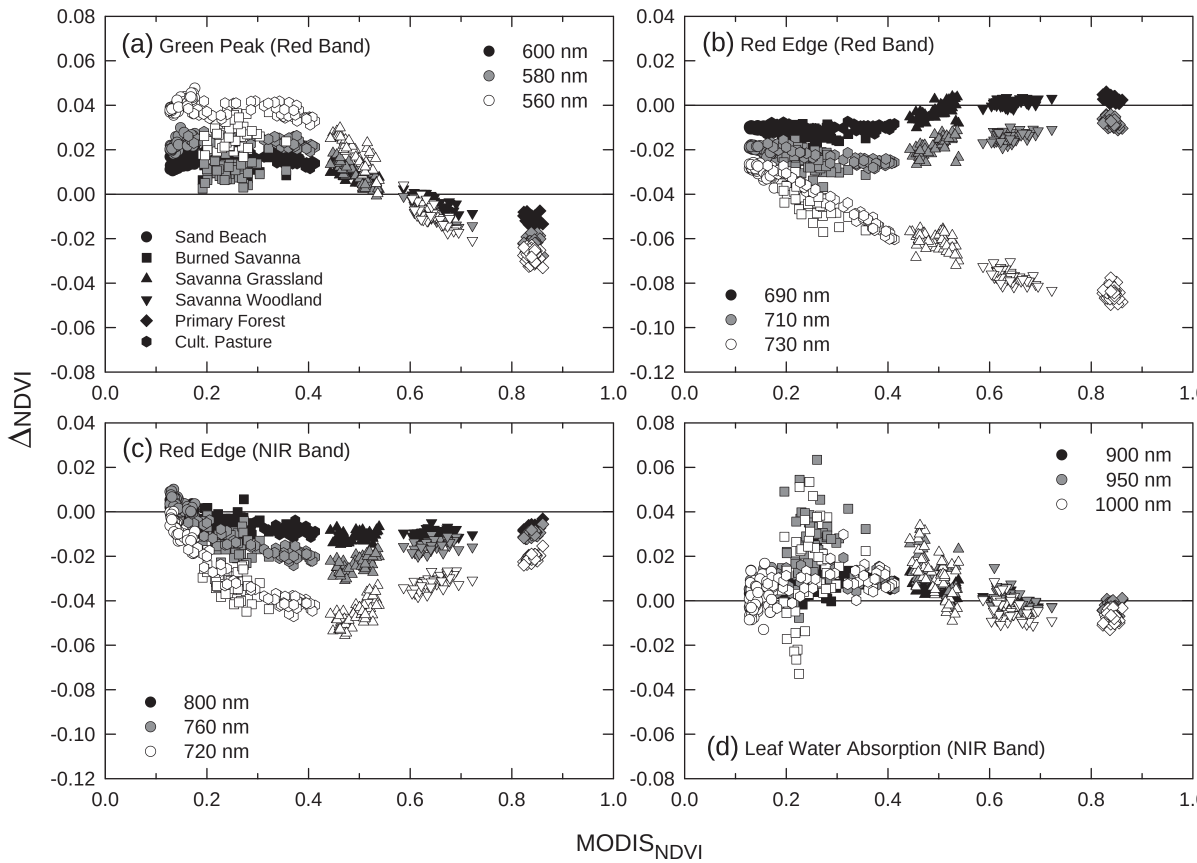

Fig. 5. Same as Fig. 4, but for the NDVI.

that the NDVI sensitivities to green vegetation change drastically when the red and NIR bands include the red edge region.

In comparison with Fig. 3, the above results can be interpreted and summarized as follows:

1) The positive differences in AVHRR vs. ETM+ NDVIs for lower NDVI values are due to the inclusion of the green peak region into AVHRR channel 1.
2) The near-linear increase in the NDVI differences, with increasing NDVI for AVHRR vs. MODIS and AVHRR vs. ETM+ is caused by the inclusion of both the green peak and red-NIR transitional regions into AVHRR channel 1.
3) The inclusion of the red-NIR transitional region into both the ETM+ red and NIR bands is responsible for the nonlinear trend observed in the NDVI differences for ETM+ vs. MODIS.

3.3.3. Percent relative differences

The computed percent relative differences are plotted against the wavelengths up to which the simulated bandpasses were widened from the MODIS bandpasses (Fig. 7). Among the land cover types, the NDVI for the bright, sand beaches was the most sensitive to increasing the red bandwidth (Fig. 7a). As the bandpass was widened to include the green peak and red edge regions, the relative differences for the sand beach target increased linearly in the positive and negative directions, respectively, reaching 28% at 560 nm and −26% at 750 nm. For the forest target, by contrast, inclusion of the green peak region caused the relative difference to increase in the opposite (negative) direction to that observed for the sand beach target and to a much lesser degree (Fig. 7a). As the bandpass was widened to include the red edge region, the differences increased nonlinearly with a maximum difference of −26% at 750 nm. These linear and nonlinear changes in the NDVI for bare soil and green vegetation have also been reported by Galvao et al. (1999) for Brazilian tropical savanna. The NDVI for the other targets showed sensitivities somewhere between these two extremes, with the NDVI for the greener targets showing behavior more similarly to the forest NDVI than the beach NDVI (Fig. 7a). It should be noted that it was only when the red bandpass was extended to 750 nm where the relative NDVI differences became almost the same for all of the targets (Fig. 7a). The NDVI sensitivities showed the greatest land cover dependency when the red bandpass was extended to 560 and 710 nm.

The sensitivities of the NDVI to the inclusion of the red edge region in the NIR band were similar to those for the red band in that the relative differences increased negatively as the bandwidth was increased toward the red edge region (Fig. 7b). The NDVI for burned savanna showed the largest sensitivity to the inclusion of the red edge, whereas those for the forested areas showed the smallest sensitivity. The relative difference for the sand beaches showed a different trend as the band was widened toward the red edge region; it initially increased positively and then turned to the negative direction (Fig. 7b).

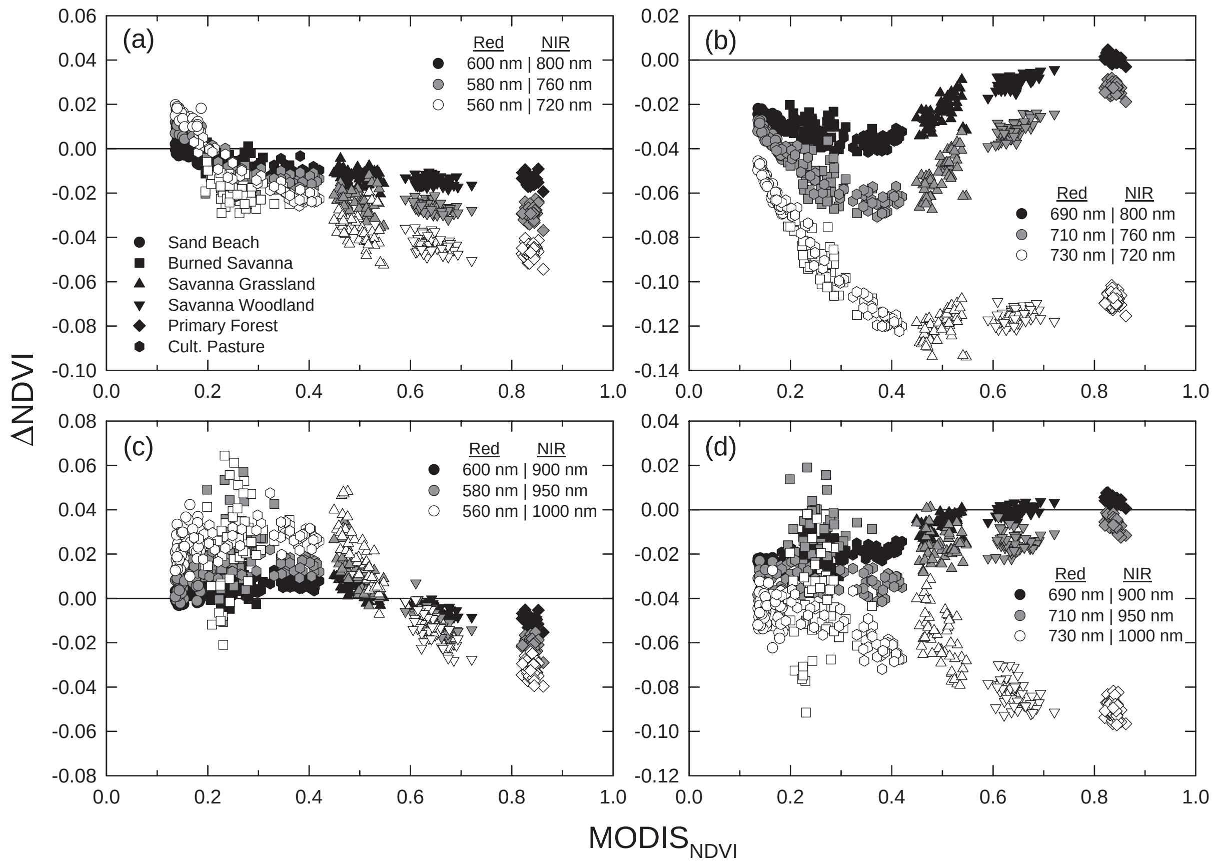

Fig. 6. Differences between NDVI computed from reflectances of widened red and NIR bandpasses and that of MODIS. The values in the legends are the wavelengths up to which the simulated bandpasses were widened from the MODIS bandpasses. NDVI differences for riparian forests which were nearly identical to those for primary forests are not shown for clarity.

This unique sensitivity behavior is due to the broad absorption feature of this land cover type at around 830 nm from iron oxide minerals (see Fig. 1) (Clark et al., 1990). The NDVI was the least sensitive to the inclusion of the leaf liquid water absorption feature. The relative differences were all less than 5%, except for the burned savanna targets, which showed higher sensitivity most likely due to the low signal-to-noise ratio of the Hyperion data. These generic trends in the NDVI

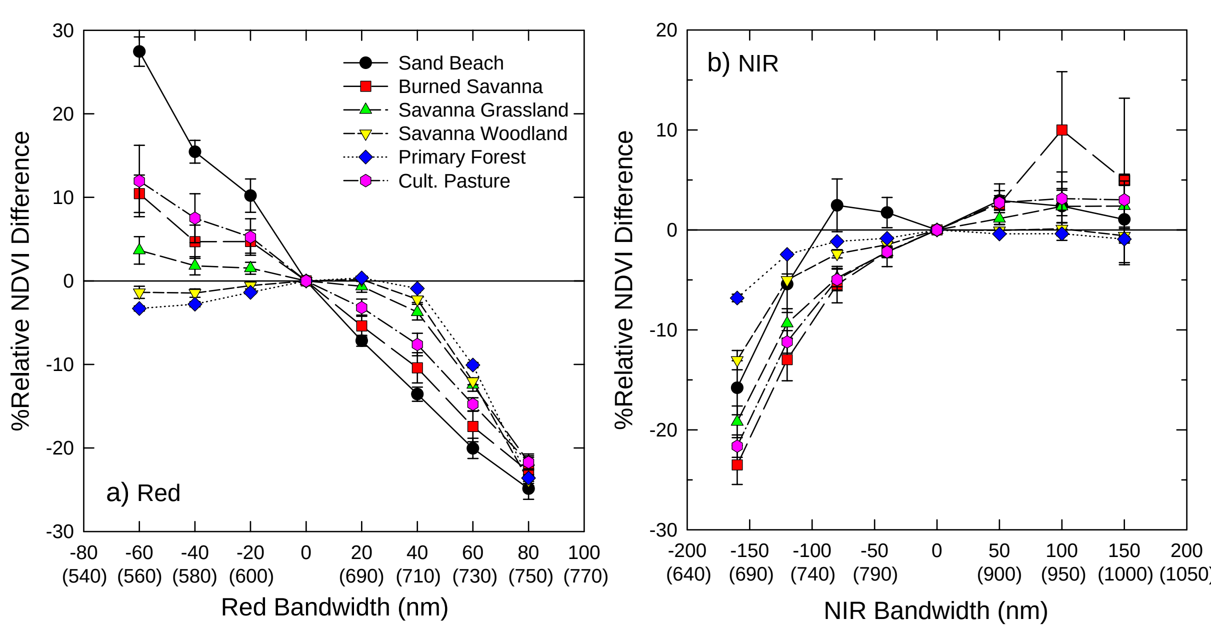

Fig. 7. Percent relative differences of the NDVI. See the text for the definition of percent relative differences.

Table 3
Estimated translation (absolute spectral correction) equations for red and NIR spectral bands, and for NDVI

Sensor		Red		NIR		NDVI	
		Dependent: $\Delta\rho=\rho_{FROM}-\rho_{TO}$		Dependent: $\Delta\rho=\rho_{FROM}-\rho_{TO}$		Dependent: $\Delta NDVI=NDVI_{FROM}-NDVI_{TO}$	
		Independent: $NDVI_{FROM}$		Independent: $NDVI_{FROM}$		Independent: $NDVI_{FROM}$	
From:	To:	Correction equation	R^2	Correction equation	R^2	Correction equation	R^2
AVHRR	MODIS	$-.0030+.0198x+.0037x^2$	.97	$-.0038-.0081x-.0263x^2$	.81	$.0174-.2091x+.0739x^2$	.97
ETM+	MODIS	$.0151-.0431x+.0287x^2$	.76	$-.0041-.0186x+.0115x^2$	.39	$-.0331-.0498x+.1090x^2$	.88
AVHRR	ETM+	$-.0204+.0740x-.0361x^2$	.94	$-.0007+.0153x-.0423x^2$	.89	$.0467-.1303x-.0889x^2$	.98

changes due to the red edge and leaf water absorption were also observed in the AVIRIS-based simulation studies conducted by Teillet et al. (1997) for British Columbia forest and Galvao et al. (1999) for Brazilian tropical savanna.

The NDVI sensitivity to bandwidth changes showed land cover dependencies. It was only when the red bandpass was extended to 750 nm (the red-NIR transitional region) that similar NDVI changes were observed for all land cover types,

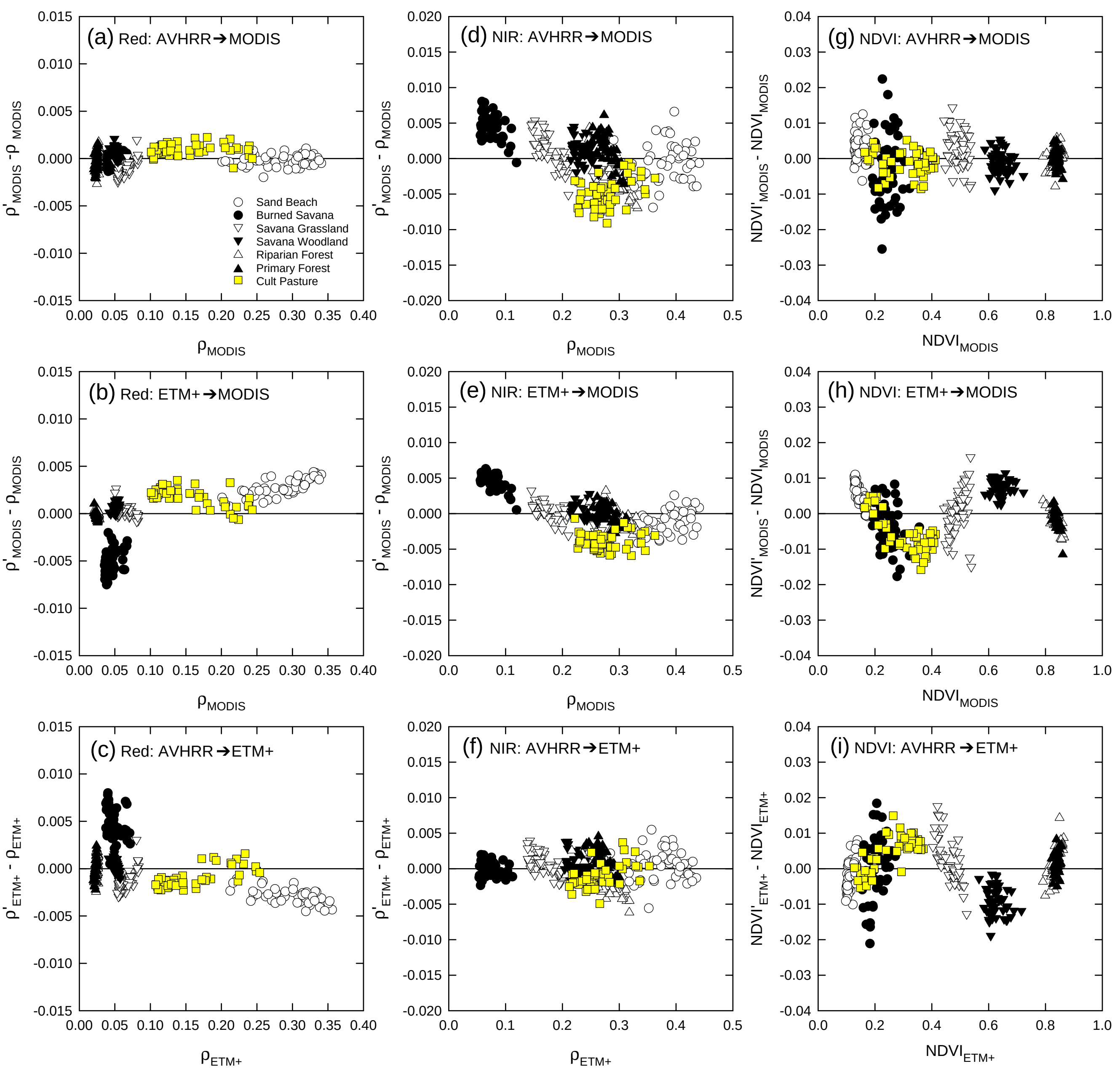

Fig. 8. Residuals after spectral corrections (translations).

resulting in a linear NDVI-to-NDVI relationship. In summary, the non-unique patterns observed in the overall inter-sensor NDVI relationships can be attributed to differential sensitivities of the NDVI to spectral bandpasses among land cover types.

3.4. Evaluation of selected empirical methods

3.4.1. Spectral corrections

The results of the least squares fittings are summarized in Table 2. Based on R^2 values, good correction equations were obtained for the translations of AVHRR channel 1 data to the MODIS and ETM+ counterparts as well as for the translations of AVHRR NDVI to the MODIS and ETM+ NDVI ($R^2 \geq .94$). The poorest result was obtained for translation of the ETM+ NIR band to the corresponding MODIS band ($R^2 = .39$). The range of R^2 values obtained in this study (.39–.98) was comparable to that reported by Trishchenko et al. (2002) (.21–.97) (Table 3).

The differences (residuals) between the translated values and those of the target sensors are plotted against the target sensor values in Fig. 8. Regardless of the R^2 values, the residuals from all the corrections are small (within ±.01 for the reflectances and ±.025 for the NDVIs). The magnitude of residuals from the ETM+ to MODIS NDVI translation (±.02 NDVI unit, i.e., ~2% precision) was comparable to 1–2% precision reported by Steven et al. (2003). Most of the translation results, however, show a bias for particular land cover types (Fig. 8). The red reflectance translation results from ETM+ to MODIS and from AVHRR to ETM+ showed large bias errors for dark, burned savanna targets (Fig. 8b,c). For the NIR reflectance translations from AVHRR and ETM+ to MODIS, bias errors are seen not only for the burned savanna, but also for the bright vegetated pastures (Fig. 8d,e). Bias errors for the NDVI translations involving the ETM+ sensor appear as nonlinear trends in the residuals (Fig. 8h,i). Thus, a higher order polynomial may be needed to obtain more accurate spectral corrections of the NDVI for these particular sensor pairs.

Overall, for the datasets used in this study, the best results (large R^2 values and small bias errors) were obtained for the translations of AVHRR to MODIS NDVI (Fig. 8g) and AVHRR to ETM+ NIR reflectance (Fig. 8f).

3.4.2. Weighted averages

In Fig. 9a, differences between $NDVI_{green+red}$ and $NDVI_{AVHRR}$ for α values of 0, .15, and 1 are plotted against $NDVI_{AVHRR}$. For $\alpha = 0$, the differences increased nearly linearly with increasing $NDVI_{AVHRR}$ values as described above (see

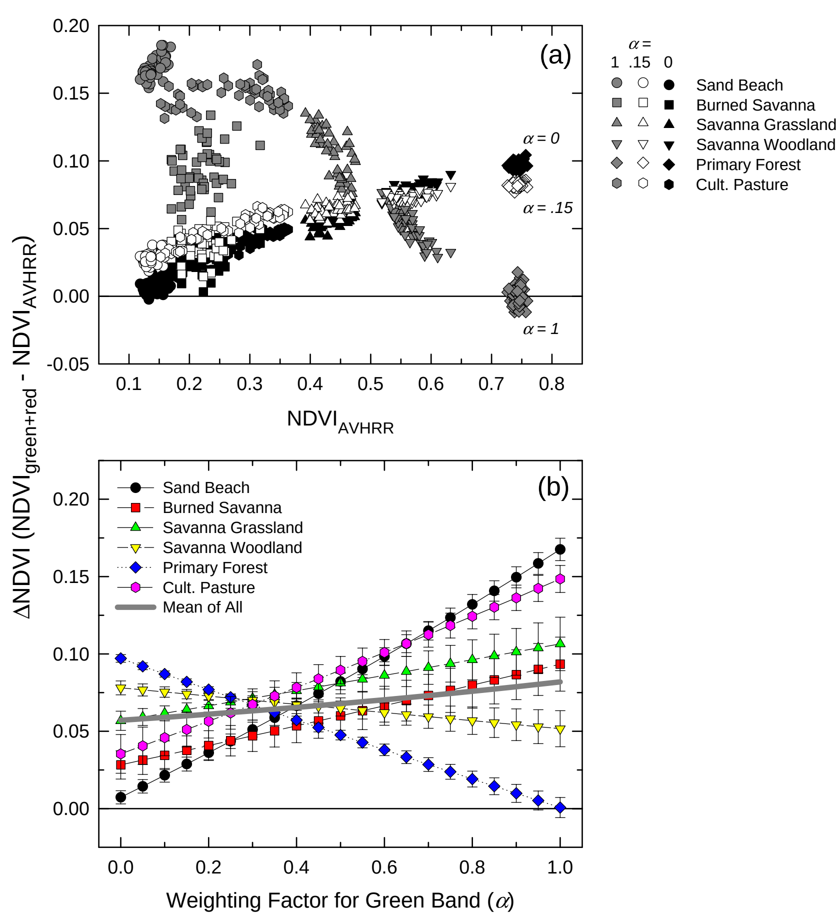

Fig. 9. Differences between $NDVI_{green+red}$ and AVHRR NDVI. In (a), the differences for α values of 0, .15, and 1 are plotted against AVHRR NDVI. In (b), mean differences along with error bars (±1 standard deviation) for each land cover type for various α values are plotted against α. The mean differences for riparian forests which were nearly identical to those for primary forests are not shown for clarity. See the text for the definition of $NDVI_{green+red}$.

Fig. 3a). When the weight was completely shifted to the green channel ($\alpha = 1$), the differences decreased nonlinearly with increasing $NDVI_{AVHRR}$ values, reaching zero on average at the highest NDVI values of .75 for the forest targets. The differences for burned savanna targets were smaller than those for the other targets with the similar NDVI values, providing clear evidence of a strong land cover dependency in the optimum weighting factor values. Setting α to the reported optimum value of .15 did not reduce the bias error (i.e., discontinuity); it merely increased and decreased the differences for index values smaller and larger than .5, respectively (Fig. 9a).

In Fig. 9b, mean differences computed for each land cover type are plotted against α values. There was no optimum weighting factor value that minimized the differences for all land cover types simultaneously. For forest and savanna woodland, the differences decreased as a more weight was given to the green band ($\alpha = 1$), whereas for the other land cover types they were the smallest when maximum weighting was given to the red band ($\alpha = 0$). For the present dataset covering tropical areas, $\alpha = 0$ (i.e., the red band) was found to be the optimum value, resulting in the smallest global mean difference (Fig. 9b).

4. Discussion and conclusions

In this paper, we empirically investigated the effects of spectral bandpass differences on inter-sensor relationships of the NDVI and reflectances. The NDVI and reflectance relationships among the sensors were neither linear nor unique and were found to exhibit complex patterns and dependencies on bandpasses. The reflectance relationships showed strong land cover dependencies. In contrast, the NDVI relationships did not show land cover dependencies, but resulted in nonlinear forms. From the sensitivity analysis conducted, the green peak region at around 550 nm and the red-NIR transitional region from 680 to 780 nm were found to be the key factors in producing the nonlinear patterns. In particular, differences among the sensors in the extents to which their red and/or NIR bandpasses covered these features significantly influenced the trends and the degrees of nonlinearity in the relationships. Consequently, simply taking a weighted average of several MODIS narrow bands did not give an adequate approximation of the broad AVHRR band response for VI continuity purposes because the narrow bands used did not include certain parts of the green peak and red-NIR transitional regions covered by the broad band. These results indicate that the NDVI and reflectance relationships need to be examined first for each combination of sensors and that the developed translation equations and coefficients will only be applicable to the specific sensor pair for which they were derived. The results also indicate that the near-linear relationship obtained for AVHRR vs. MODIS NDVI was the result of mere chance and that nonlinear relationships should be expected for most sensor pairs.

The empirical spectral correction method performed well. NDVI-based quadratic functions flexibly modeled most of the nonlinear patterns, reducing inter-sensor NDVI and reflectance differences by 80% (.1 to .02) and 65% (.03 to .01), respectively, for the best case. However, many of the translation results suffered from land cover-dependent bias errors. The reflectance results indicated the need to explicitly account for both greenness and brightness effects to further reduce these bias errors, whereas those for the NDVI showed the need of higher order polynomials to more accurately model the inter-sensor relationships. Our empirical results justify the theoretical approach proposed by Yoshioka et al. (2003), whereby vegetation isoline equations originally developed to model the behavior of red vs. NIR reflectances were applied to red vs. red and NIR vs. NIR reflectances between two sensors. As vegetation isolines are formed by connecting reflectance values of constant greenness over variable canopy background brightness, isoline-based approaches that explicitly consider and model both target greenness and brightness may give a better mechanistic understanding and predictive modeling of cross-sensor relationships for reflectances as well as the NDVI.

Regardless of the translation methods used, the results are likely to be contaminated by bias errors because observations from different spectral bands are inherently different. Thus, translated data will have to be inputted into downstream algorithms such as land cover classification algorithms, biogeochemical cycle models, and climate models, and the degree to which bias errors have been reduced will need to be determined through comparisons of the outputs of these downstream algorithms. True continuity/compatibility of NDVI and reflectance data from different sensors will only have been achieved when the outputs of these downstream algorithms become the same regardless of whether translated data or the corresponding target sensor data are used as inputs.

The analyses presented here were limited to the ground-level with nadir viewing and constant solar zenith angles. Other factors, including atmospheric contaminations as well as bidirectional reflectance distribution functions, certainly affect inter-sensor NDVI and reflectance relationships because the effects of these factors are strongly wavelength-dependent (e.g., Cihlar et al., 2001; Maignan et al., 2004). For example, atmospheric column water vapor contents strongly lower the AVHRR channel 2, whereas the MODIS NIR band avoids this wavelength region (Salomonson et al., 1989). Research into the influences of a coupled atmosphere–surface system on cross-sensor relationships is currently in progress.

Acknowledgements

The authors would like to thank three anonymous reviewers for their valuable suggestions and comments in improving the manuscript. The authors would also like to thank personnel of EMBRAPA-Cerrado, Federal University of Goias, University of Brasilia, and the LBA project office for their logistical support and assistance in the field assessment. This work was supported by a NASA EOS grant NNG04GL88G, NASA EO-1 grant NCC5-478, and NASA MODIS contract NAS5-31364.

References

Biggar, S. F., Thome, K. J., & Wisniewski, W. (2003). Vicarious radiometric calibration of EO-1 sensors by reference to high-reflectance ground targets. *IEEE Transactions on Geoscience and Remote Sensing*, *41*(6), 1174–1179.

Bryant, R., Moran, M. S., McElroy, S. A., Holifield, C., Thome, K. J., Miura, T., et al. (2003). Data continuity of Earth Observing 1 (EO-1) Advanced Land Imager (ALI) and Landsat TM and ETM. *IEEE Transactions on Geoscience and Remote Sensing*, *41*(6), 1204–1214.

Che, N., & Price, J. C. (1992). Survey of radiometric calibration results and methods for visible and near infrared channels of NOAA-7,-9, and -11 AVHRRs. *Remote Sensing of Environment*, *41*(1), 19–27.

Cihlar, J., Denning, S., Ahern, F., Arino, O., Belward, A., Bretherton, F., et al. (2002). Initiative to quantify terrestrial carbon sources and sinks. *EOS Transactions*, *83*(1), 1.

Cihlar, J., Tcherednichenko, I., Latifovic, R., Li, Z., & Chen, J. (2001). Impact of variable atmospheric water vapor content on AVHRR data corrections over land. *IEEE Transactions on Geoscience and Remote Sensing*, *39*(1), 173–180.

Clark, R. N., King, T. V. V., Klejwa, M., Swayze, G. A., & Vergo, N. (1990). High spectral resolution reflectance spectroscopy of minerals. *Journal of Geophysical Research*, *95*(B8), 12,653–612,680.

Dong, J. R., Kaufmann, R. K., Myneni, R. B., Tucker, C. J., Kauppi, P. E., Liski, J., et al. (2003). Remote sensing estimates of boreal and temperate forest woody biomass: Carbon pools, sources, and sinks. *Remote Sensing of Environment*, *84*(3), 393–410.

Gallo, K., Ji, L., Reed, B., Dwyer, J., & Eidenshink, J. (2004). Comparison of MODIS and AVHRR 16-day normalized difference vegetation index composite data. *Geophysical Research Letters*, *31*(7), L07502.

Galvao, L. S., Vitorello, I., & Filho, R. A. (1999). Effects of band positioning and bandwidth on NDVI measurements of tropical savannas. *Remote Sensing of Environment*, *67*(2), 181–193.

Gao, B. -C. (2000). A practical method for simulating AVHRR-consistent NDVI data series using narrow MODIS channels in the 0.5–1.0 μm spectral range. *IEEE Transactions on Geoscience and Remote Sensing*, *38*(4), 1969–1975.

Gesch, D. B. (1994). Topographic data requirements for EOS global change research. *U.S. Geological Survey Open-File Report*, *94-626*.

Gitelson, A. A., & Kaufman, Y. J. (1998). MODIS NDVI optimization to fit the AVHRR data series-spectral considerations. *Remote Sensing of Environment*, *66*(3), 343–350.

Goward, S. N., Markham, B., Dye, D. G., Dulaney, W., & Yang, J. (1991). Normalized difference vegetation index measurements from the advanced very high resolution radiometer. *Remote Sensing of Environment*, *35*(2–3), 257–277.

Green, R. O., Pavri, B. E., & Chrien, T. G. (2003). On-orbit radiometric and spectral calibration characteristics of EO-1 Hyperion derived with an underflight of AVIRIS and in situ measurements at Salar de Arizaro, Argentina. *IEEE Transactions on Geoscience and Remote Sensing*, *41*(6), 1194–1203.

Huete, A., Didan, K., Miura, T., Rodriguez, E. P., Gao, X., & Ferreira, L. G. (2002). Overview of the radiometric and biophysical performance of the MODIS vegetation indices. *Remote Sensing of Environment*, *83*(1–2), 195–213.

Kaufman, Y. J., & Holben, B. N. (1993). Calibration of the Avhrr visible and near-Ir bands by atmospheric scattering, ocean glint and desert reflection. *International Journal of Remote Sensing*, *14*(1), 21–52.

King, M. D., Menzel, W. P., Kaufman, Y. J., Tanre, D., Gao, B. -C., Platnick, S., et al. (2003). Cloud and aerosol properties, precipitable water, and profiles of temperature and water vapor from MODIS. *IEEE Transactions on Geoscience and Remote Sensing*, *41*(2), 442–458.

Maignan, F., Breon, F. -M., & Lacaze, R. (2004). Bidirectional reflectance of Earth targets: Evaluation of analytical models using a large set of spaceborne measurements with emphasis on the hot spot. *Remote Sensing of Environment*, *90*(2), 210–220.

Myneni, R. B., Keeling, C. D., Tucker, C. J., Asrar, G., & Nemani, R. R. (1997). Increased plant growth in the northern high latitudes from 1981 to 1991. *Nature*, *386*(6626), 698–702.

Pearlman, J. S., Barry, P. S., Segal, C. C., Shepanski, J., Beiso, D., & Carman, S. L. (2003). Hyperion, a space-based imaging spectrometer. *IEEE Transactions on Geoscience and Remote Sensing*, *41*(6), 1160–1173.

Salomonson, V. V., Barnes, W. L., Maymon, P. W., Montgomery, H. E., & Ostrow, H. (1989). MODIS—advanced facility instrument for studies of the Earth as a system. *IEEE Transactions on Geoscience and Remote Sensing*, *27*(2), 145–153.

Steven, M. D., Malthus, T. J., Baret, F., Xu, H., & Chopping, M. J. (2003). Intercalibration of vegetation indices from different sensor systems. *Remote Sensing of Environment*, *88*(4), 412–422.

Teillet, P. M., Staenz, K., & William, D. J. (1997). Effects of spectral, spatial, and radiometric characteristics on remote sensing vegetation indices of forested regions. *Remote Sensing of Environment*, *61*(1), 139–149.

Trishchenko, A. P., Cihlar, J., & Li, Z. (2002). Effects of spectral response function on surface reflectance and NDVI measured with moderate resolution satellite sensors. *Remote Sensing of Environment*, *81*(1), 1–18.

Tucker, C. J. (1979). Red and photographic infrared linear combinations for monitoring vegetation. *Remote Sensing of Environment*, *8*, 127–150.

Ungar, S. G., Pearlman, J. S., Mendenhall, J. A., & Reuter, D. (2003). Overview of the Earth Observing One (EO-1) mission. *IEEE Transactions on Geoscience and Remote Sensing*, *41*(6), 1149–1159.

Vermote, E. F., Tanre, D., Deuze, J. L., Herman, M., & Morcrette, J. J. (1997). Second simulation of the satellite signal in the Solar Spectrum, 6S: An overview. *IEEE Transactions on Geoscience and Remote Sensing*, *35*(3), 675–686.

Yoshioka, H., Miura, T., & Huete, A. R. (2003). An isoline-based translation technique of spectral vegetation index using EO-1 Hyperion data. *IEEE Transactions on Geoscience and Remote Sensing*, *41*(6), 1363–1372.

Yoshioka, H., Miura, T., Huete, A. R., & Ganapol, B. D. (2000). Analysis of vegetation isolines in red-NIR reflectance space. *Remote Sensing of Environment*, *74*(2), 313–326.

Zhang, X., Friedl, M. A., Schaaf, C. B., Strahler, A. H., Hodges, J. C. F., Gao, F., et al. (2003). Monitoring vegetation phenology using MODIS. *Remote Sensing of Environment*, *84*(3), 471–475.